

Widening Viewing Angles of Automultiscopic Displays using Refractive Inserts

Geng Lyu, Xukun Shen, Taku Komura, Kartic Subr and Lijun Teng

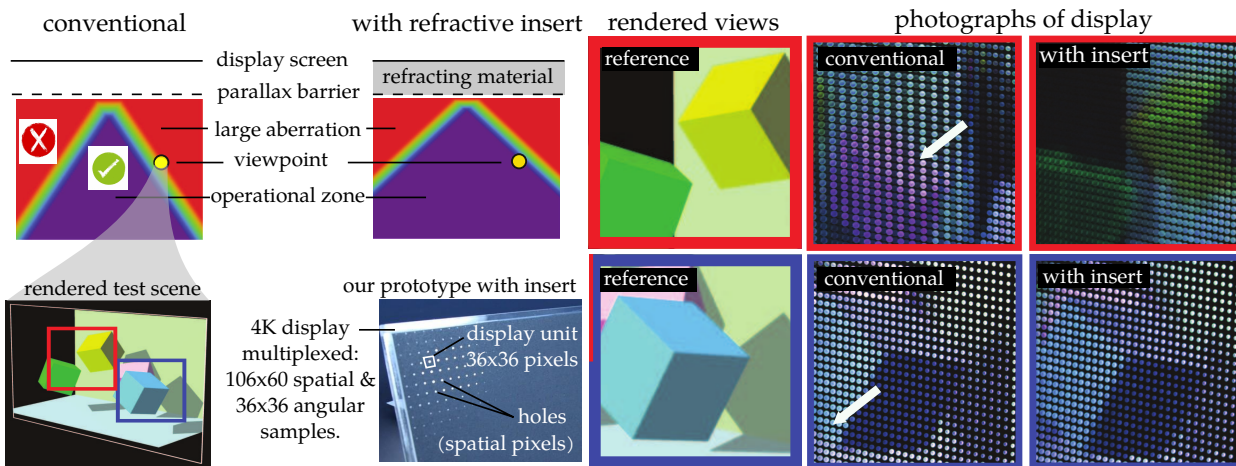


Figure 1: The viewing angle of automultiscopic displays, that use parallax barriers, can be extended by inserting a refracting medium between the screen and barrier. The figure shows a test scene and compares photographs of the display with and without inserts. The viewing position is chosen to be at the boundary of the safe viewing zone of a conventional display (top view). Considerable aberrations are observed (white arrows) in the conventional solution. These errors are not present when refractive inserts are used (rightmost). Our prototype performs spatio-angular multiplexing of a 3840×2160 screen to achieve an angular resolution of 36×36 and a spatial resolution of approximately 106×60 (hence the prominent pixels in the photographs). Please see accompanying video.

Abstract— Displays that can portray environments that are perceivable from multiple views are known as multiscopic displays. Some multiscopic displays enable realistic perception of 3D environments without the need for cumbersome mounts or fragile head-tracking algorithms. These *automultiscopic* displays carefully control the distribution of emitted light over space, direction (angle) and time so that even a static image displayed can encode parallax across viewing directions (lightfield). This allows simultaneous observation by multiple viewers, each perceiving 3D from their own (correct) perspective. Currently, the illusion can only be effectively maintained over a narrow range of viewing angles. In this paper, we propose and analyze a simple solution to widen the range of viewing angles for automultiscopic displays that use parallax barriers. We propose the use of a refractive medium, with a high refractive index, between the display and parallax barriers. The inserted medium warps the exitant lightfield in a way that increases the potential viewing angle. We analyze the consequences of this warp and build a prototype with a 93% increase in the effective viewing angle.

Index Terms—Automultiscopic displays, lightfields

1 INTRODUCTION

The effectiveness of a virtual reality (VR) system hinges on the display technology used [37, 38]. Head-mounted stereoscopic displays are currently considered to be the default choice for VR experiences. Despite being cumbersome, lacking spatial display resolution and requiring precise tracking of head pose, they are popular for individual interactive experiences because they enable immersion and depth perception. However, they are not suited to situations requiring simultaneous experiences by multiple viewers, such as a family in a living room or an audience in a cinema hall. Displays which inherently depict the spatio-angular distribution of light are useful since viewers may natu-

rally explore a range of perspectives without needing special sensors or algorithms to track their positions. Such *auto-multiscopic* displays have been studied widely in the literature [16, 53]. Some auto-multiscopic displays are optimized to be auto-stereoscopic [10] to each viewer thus enabling them to perceive depth due to parallax across the left and right eye positions, from their unique view.

Auto-multiscopy can be achieved by either using an inherently volumetric display [12], which produces a spatio-directional-temporal display, or by using a 2D display and optical elements that redistribute light energy across space, direction and time. The latter can further be divided into *parallax-based* and *holographic* displays. Parallax-based displays produce lightfields using light-directing optical elements placed strategically in front of a 2D display. Holographic displays use 2D elements to generate tailored wavefronts by exploiting diffraction of coherent light. In this paper, we only consider parallax-based auto-multiscopic displays.

The simplest parallax-based auto-multiscopic display [3, 21] consists of a 2D display in front of which an opaque screen, containing an array of carefully chosen slits (or holes). The pattern of holes encodes pixels that will be visible from each viewing position. There are two problems introduced by using this mechanism for ray selection: Decreased light efficiency since most of the light from the display is blocked by the

- Geng Lyu is with Beihang University and IPAB of University of Edinburgh. E-mail: lvgengbuaa@gmail.com.
- Xunkun Shen is with Beihang University. E-mail: xkshen@buaa.edu.cn.
- Taku Komura is with IPAB at University of Edinburgh. E-mail: tkomura@ed.ac.uk.
- Kartic Subr is with IPAB at University of Edinburgh. E-mail: kartic@ed.ac.uk.
- Lijun Teng is with Institute of Micro and Nano System at University of Edinburgh. E-mail: L.Teng@ed.ac.uk.

barrier; and second, the range of viewing angles is limited (see figure 2). The former may be avoided by the use of integral imaging (lenslet arrays [44] or lenticular sheets [39]). In this paper, we address the latter problem, of limited viewing angles, and propose and analyze a simple solution to increase the viewing angle of auto-multiscopic displays that use parallax-barriers.

We analyze the effect of refractive media placed between the display screen and parallax barrier. Refraction at the hole causes light to bend away from the normal as they exit the barrier. Since the incident and refracted angles are related nonlinearly (by Snell’s law), its analysis is non-trivial. The nonlinearity is more pronounced when inserts with high refractive indices are used, which also raises the question of how the refractive index should be chosen. Further, there are complex trade offs between extension of the view angle and other aberrations such as blur which need to be carefully analyzed.

In this paper, we show that lightfields emanating from automultiscopic displays with refractive inserts have the same spatial bandwidth as without inserts, but that the angular bandwidths are scaled down by the refractive index of the insert. We derive that inserts can achieve wider viewing angles and more uniform angular sampling of the lightfield. We describe how the refractive index of inserts may be chosen to optimally avoid *crossstalk* between neighbouring pinholes by exploiting total internal reflection. We propose a simple modification to existing rendering algorithms, to accommodate refractive inserts. Finally, we build a prototype and demonstrate that the viewing angle is 90% wider than without the insert. The resulting images from our prototype do not contain objectionable artifacts observable in conventional displays, despite the theoretical prediction of blur being higher for our approach.

The goal of this work is to demonstrate the effectiveness of refractive inserts. Several other methods have been proposed to improve conventional displays. We believe that those works are complementary to this work and can possibly be combined in future work. The main contributions of this paper are:

1. we show that the use of refractive inserts leads to more uniform angular sampling of the exitant lightfield;
2. we present a frequency analysis of the lightfield warped by refractive inserts which shows that inserts scale down angular bandwidth;
3. we demonstrate that the use of refractive inserts can improve the viewing angle significantly (by 90% in our prototype); and
4. we propose a simple modification to an existing rendering algorithm, which accommodates for refraction at the pinholes.

2 RELATED WORK

2.1 Auto-multiscopic displays

Parallax-barriers and integral imaging: Occlusion by parallax barriers [21] is a useful way to achieve spatio-angular multiplexing from pixels on a regular (spatial) display. The resulting lightfield [14] encodes parallax and therefore enables automultiscopic viewing [17]. Since those early works, there has been extensive study of this area [10, 19, 26, 39]. When an opaque barrier with transmitting holes is placed at some distance in front of a display screen, the location of the viewer determines the pixels that will be visible. If the image rendered on the screen is strategically chosen by accounting for the relative positions of holes, the observed parallax remains consistent across views and produces a perception of depth (3D) (see fig. 3b). The transition across views can be optimized using sheared filtering [8]. Unlike autostereoscopic displays [16], which provide the same stereo illusion from multiple view locations (see fig. 3a), auto-multiscopic displays project multiple different views. Two major limitations of these methods is that they offer a narrow zone within which the parallax is consistent and that they are not light efficient since a large fraction of the light from the screen is blocked by the barrier. The latter is mitigated by the use of small lenses at each hole. This is typically done by the use of an array of microlenses [34]. There has been a large amount of work in this area [27] especially for capturing and reproducing focal cues. Typically, initial analysis is performed on a micro-hole array and lenses

are later considered during engineering of the display to improve light efficiency.

Other methods: Besides ray selection using barriers, another way to achieve the perception of depth is to orchestrate wavefronts of light so that their interactions provide a compelling and consistent observable parallax. In holography, the wavefronts are generated by diffraction of coherent light through tiny holes [35]. There has been a large amount of work recently on both computer-generated holograms [41] and compressive light field displays [30]. All the above methods assume that the display substrate consists of 2D pixels. Volumetric displays, on the other hand, can be used to display 3D information naturally [12, 36]. They are capable of providing full 360° parallax, but are typically expensive and bulky [42]. There are a range of methods that strike a compromise between full 3D displays and 2D displays achieving parallax. e.g. directional backlights with Fresnel lens elements [40], multilayered displays [49], guided-wave illumination [11]. Of these, many exploit time division multiplexing and therefore require high-speed elements. Layered displays based on polarization fields [28] or additive effects [48] can generate high quality light fields but with limited viewing angle (due their optical structure).

Perception and analysis: Inconsistent stereoscopic images result in undesirable perceptual artifacts [13], often called ‘ghosting’. This could either be caused by incompatible stereoscopic content [25] or due to imperfections in the display system. Typically, errors are analyzed in the resulting binocular disparity using lightfield theory [15]. Although disparity remapping is less relevant for an automultiscopic display, aberrations in the displayed lightfield (and hence parallax) will lead to perceptual inconsistencies [45]. Typical tools for the analysis of lightfield displays include viewing zone analysis of multi-view display [7] and frequency domain analysis [18], which have resulted in improvements for antialiasing of automultiscopic displays [53], content adaptive lenticular [43] prints, etc. Lightfields have been analyzed from the perspective of computational photography [31], computer vision [47] and in rendering [4, 9, 33].

2.2 Light field imaging and rendering

Plenoptic imaging and lightfield parameterization: The plenoptic function [1] captures the distribution of visible light energy across position, angle, time and wavelength. The spatio-angular ($3D \times 2D$) distribution (and sometimes temporal) is commonly studied in the computer graphics literature. The dimensionality of the phase space is further reduced by only studying light emanating from the convex hull of a given space, since all points along a ray’s direction will then encode the same radiant light energy. Considering most light field imaging and display systems are only concerned with the light field within some convex region of space, the 5D phase space of the light field is usually simplified to 4D [32] which can be parameterized in several ways. Popular methods include the coordinates (STUV) of intersection of rays with two fixed planes [32], a point on a 2D manifold and a direction (surface lightfields) and spherical coordinates [24]. STUV coordinates are simple to analyze and practical when dealing with systems such as flat displays which do not need to be analyzed for views from all around [52]. They also allow interpretation of the 4D lightfield tensor as a 2D array of 2D images. We refer to each of the sub-images as a *display unit* in this paper.

Rendering and processing: The process of determining the colored radiance values for each pixel in a view (slice) of a discretised (4D) lightfield is called rendering. Views may be rendered from acquired lightfields [23], from video [46] or by simulating or approximating light transport from 3D models. In this paper we test our display using rasterised renders of specially designed scenes, which can either be achieved via multi-view perspective rendering (MVPR) [44] or parallel group rendering (PGR) [50]. MVPR renders several high-resolution key views followed by view interpolation using these views. Two problems with this approach are that many rendering passes, one for each display unit (also called screenlet or subview), are required and that high-quality view interpolation from sparse views remains an open

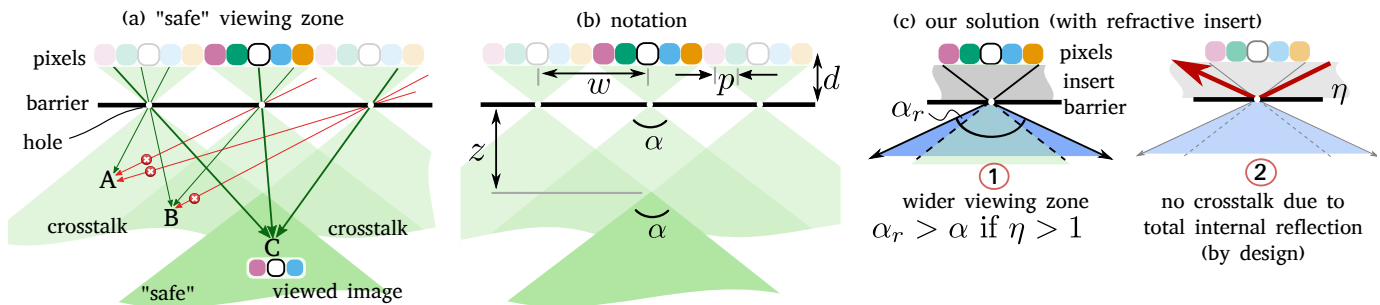


Figure 2: A visualization of the “safe” viewing zone (a) of an automultiscopic display with a spatial resolution of 3 pixels (3 holes in the barrier). The angular resolution is the number of pixels in each display unit (5 pixels in this illustration). Images viewed from A and B are incorrect since they consist of rays (red) stemming from display units not associated with the corresponding holes. Placing inserts with a refractive index $\eta > 1$ between the pixels and the barrier results in a wider angular spread α_r associated with each display unit (c.1). This in turn widens the safe viewing zone. If η is chosen so that the critical angle is subtended by half the display unit, then rays causing crosstalk (red arrow in c.2) are totally internally reflected.

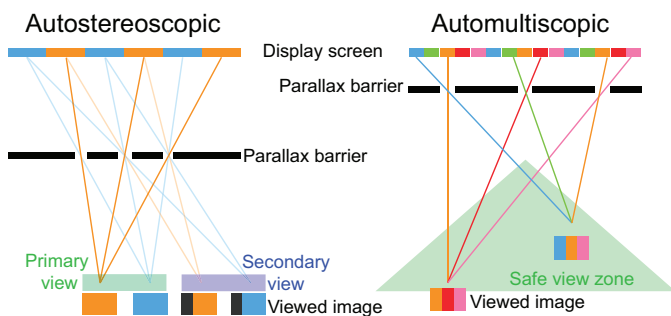


Figure 3: Left: Autostereoscopic displays provide two stereo views in its view zones. Right: Automultiscopic displays provide full motion parallax within its safe view zone.

and challenging problem. PGR exploits parallel rays across display units by rendering them together in a single pass. Therefore the number of rendering passes is the number of pixels in each display unit. Since, in our display, the number of display units (the number of holes in the barrier) is much larger than the number of pixels in each display unit, we choose PGR. We render groups of parallel rays using oblique orthographic projection and reassemble them.

2.3 Review: Automultiscopic displays with barriers

For automultiscopic displays that use micro-hole arrays as barriers, the source of light energy is a *display screen* composed of pixels and ray selection is performed via an opaque *light barrier* with a grid of holes punched in it. The barrier masks the emitted light and the *masking function* is a 2D Shah (comb) function composed of Dirac delta functions at the locations of the holes. We illustrate concepts with a 1D version of this display as shown in Figure 2.

We call the set of pixels modulated by each hole a *display unit*. The figure shows three display units each with 5 pixels. A hole along with the pixels in its display unit represents a single *spatial pixel*. We denote the width of each pixel within a display unit as p and the resolution of the display unit with R_a . Therefore, the width of each display unit is $w = pR_a$. If the distance between the light barriers and the display screen is d , then the angular spread of a spatial pixel is $\alpha = 2 \arctan \frac{w}{2d}$. By construction, the number of display units matches the number of holes in the barrier. For each view, the ray through a hole forms a single pixel in the image for the view. We denote this *spatial resolution*, or the number of holes (and hence display units), as R_s . As the viewer’s position changes, the visible ray through each hole emanates from a different pixel in the display unit. R_a can be seen as the *angular resolution* of the automultiscopic display. A viewer who is within

the angular spread of all the spatial pixels will see a perfect image consisting of R_s pixels (viewer at C in figure 2(a) with $R_s = 3$). We call this region the *operational zone* of the display. z is the minimum distance from this zone to the display plane.

Various methods have been proposed to widen the viewzone: sequentially controlled lenses [29], moving lenslet arrays with low fill factor [22] and adaptive liquid crystal prism arrays [5] are the most popular. Methods that exploit time division multiplexing have several drawbacks including low brightness, mechanical noise, bulky devices, short endurance and high cost. There has been some effort towards using transparent media for autostereoscopic displays [6, 20, 51] but they do not evaluate the idea or provide much analysis. They also do not propose solutions for rendering using such displays thereby limiting their applicability for Virtual Reality applications.

Displays with parallax barriers are plagued by four important aberrations: crosstalk, aliasing, blur and pixel-mismatch. For views outside the *operational zone* of the display, pinholes can potentially select rays that are outside its corresponding display unit. We call aberrations caused by this phenomenon *crosstalk*. *Aliasing* is caused by an inconsistency between the sampling rates of rendering and display. When pixels and pinholes have finite dimensions, they cause multiple rays to be selected for each view causing *blur*. In practice, since the barrier may not be exactly parallel to the display screen, different micro holes may be at different distances from the pixels. This warp causes objectionable artifacts which we call *pixel-mismatch* since rays are incorrectly selected for each hole.

3 REFRACTIVE INSERTS

In our prototype, we insert a sheet of refractive material (fig. 2 c) between the displayed pixels and the parallax barrier. This results in multiple benefits: (1) it widens the space of angles from which a display unit is visible through its corresponding pinhole; (2) it results in a more uniform sampling of angles; and (3) it reduces rays causing crosstalk due to total internal reflection. We analyse each of these effects in this section and also investigate the realistic case when the pinholes have finite size. Throughout this paper, we will only consider the case of a single parallax barrier with an array of holes.

3.1 Analysis: pin hole assumption

We first analyze the case with infinitesimal holes. Although this is impossible to achieve practically it serves as a simple setting (ignoring diffraction) to illustrate the effect of refractive inserts.

Refractive index: To avoid crosstalk, the refractive index of the medium must be chosen so that the angle of incidence of a ray from the edge of each display unit, at the hole, is the critical angle associated with the medium: so, $\eta = \sqrt{w/2d + 1}$. This may not always be possible due to fabrication limits of inserts with arbitrary refractive indices.

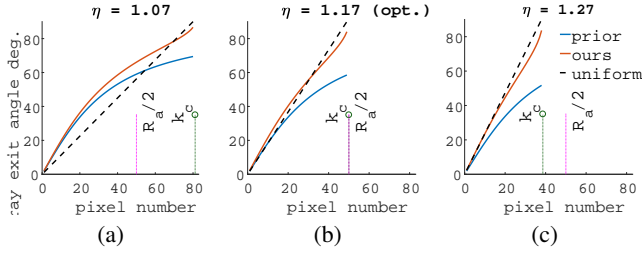


Figure 4: Angular sampling for a 4K display screen with 0.1mm between pixels and a barrier with 400 holes placed 3mm in front of the screen. i.e. each display unit is $R_a = 100$ pixels (angular samples) wide. The optimal refractive index for this case is $\eta = 1.17$ (b), and our solution (red) causes the samples to be closer to uniform (black dashed) than when no refractive insert is used (blue). k_c is the pixel number for which the incident ray to the hole is at the critical angle. Ideally we want $k_c = R_a/2$. A lower value results in crosstalk (a) while higher refractivity leads to poor utilisation of the display unit (c).

Light field resolution: The use of refractive inserts *does not change the spatial resolution* of automultiscopic displays with parallax barriers. i.e. the spatial resolution is the number of holes in the barrier. The angular resolution however is modified due to the refractive warp (according to Snell’s law) of the lightfield. In conventional displays (without refraction), uniformly spaced pixels on the screen result in non-uniform angular sampling. However, the sampling is closer to uniform angular sampling when refractive inserts are used, since rays that approach the hole (from the displayed pixels) close to normal incidence are warped less. Fig. 4 shows a plot of the outgoing angles subtended (Y-axis) by rays from each of the pixels (X-axis) in a display unit. Uniform angular sampling is achieved when the angles are linear in pixel numbers (dashed black line). However, because the pixels are spaced evenly, the conventional solution, without refraction (blue curve), results in uneven sampling (denser near the normal). Although the angular samples with refraction (red curve) are not perfect, they are closer to uniform angular sampling than without the use of inserts.

“Safe” viewing zone: We define the operational zone of the display due to the refractive insert using two parameters: distance to the barrier (z_r) and angular spread (α_r). Both these parameters are functions of the refractive index. Simple trigonometry yields

$$\alpha_r = 2 \arcsin \left(\frac{\sin(w/2d)}{\eta} \right) \quad \text{and} \quad z_r = \frac{wR_s \sin(w/2d)}{2\sqrt{\eta^2 - \sin^2(w/2d)}} \quad (1)$$

3.2 Lightfield blurring

The ideal automultiscopic display with parallax barriers consists of infinitesimal pixels and pinholes (ignoring wave effects such as diffraction). Virtual objects are perceived to have depth due to parallax across multiple view locations. When pixels and holes have finite dimensions, the displayed lightfield contains spurious rays that were either not supposed to be emitted in the first place or that were meant to be masked by the barrier. These spurious rays are aberrations that impact depth perception. In figure 5, we illustrate the extent of such aberrations with and without refractive inserts. The blur could be observed spatially (view location is perturbed), in the angular dimension (different angles for a given location), or more commonly as a combination of both.

Figure 8 illustrates transformations to lightfields through transport from the display screen (pixels) until the view location (eye). Intermediate lightfields at the barrier before the holes and after they pass through the holes in the barrier (multiplication by a masking function) are also shown. Viewing this lightfield at any spatial location results in an angular slice through the lightfield (green vertical line). The extent of blur is indicated by the spatio-angular spread of each “block” of the

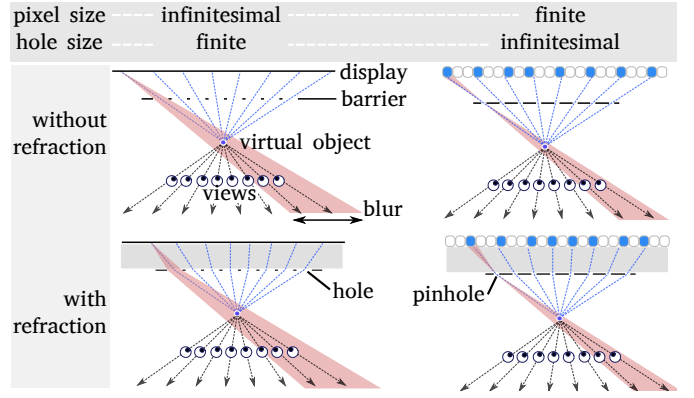


Figure 5: Finite sizes of holes in the parallax barrier (left) and pixels on the display screen (right) are two sources of blur in automultiscopic displays. The extent of blur is different in conventional displays without refraction (top) and in our proposed solution (bottom) with refractive inserts. In practice, the spatio-angular blur is caused by a combination large pixels as well as large holes.

lightfield in the rightmost column. Inserting a refracting medium between the display and the barrier introduces an additional angular warp (analyzed in sec. 3.3) between the rightmost two columns of figure 8.

Consider a scene with exactly one virtual bright object which projects to one display pixel. Although multiple angular views of this object may be rendered across display units, each display unit will only contain one lit pixel. Ideally, for each view V , the object will only be visible through one of the holes (say hole H_i). For finite sized holes however, since there is an integration over the angle subtended by the holes, parts of this object may be visible through other holes $H_{i\pm k}, k = 1, 2, \dots, k_{max}$. The blur radius at that view location can then be written as $b_V = wk_{max}$. We were unable to derive b_V analytically, but we illustrate its behavior by numerically computing it (by simulation) across view locations for an example setting (see sec. 4.2).

3.3 Frequency analysis

We present a frequency analysis of the warp introduced by refractive inserts. The analysis shows that the effect is bandlimiting in angle without any change to the spatial bandwidth. Our result supports intuition that the wider spread of the exitant lightfield, resulting in lower angular frequencies. We perform our discussion of the frequency analysis in flatland spanned by x and θ which are spatial and angular coordinates respectively. In this ray space, we denote the light field and its Fourier transform using $\ell(x, \theta)$ and $\hat{\ell}(\omega_x, \omega_\theta)$ respectively, so:

$$\hat{\ell}(\omega_x, \omega_\theta) = \int_{-\pi/2}^{\pi/2} \int_{-\infty}^{\infty} \ell(x, \theta) e^{-2\pi x \omega_x} e^{-2\pi \theta \omega_\theta} dx d\theta. \quad (2)$$

Let $\ell_P(x, \theta)$ be the lightfield at the plane of pixels P (see fig. 6.a), $\ell_{M^-}(x, \theta)$ be the incident lightfield (from P) at the plane of the mask M , $\ell_{M^+}(x, \theta)$ be the resulting lightfield at M after multiplication by the mask (barrier). The relationship between these lightfields (fig. 6.b-d) is easily obtained using as in prior work [9, 18, 53]:

$$\ell_P(x, \theta) = \ell_{M^-}(x - d \tan \theta, \theta) \quad (3)$$

$$\ell_{M^+}(x, \theta) = \ell_{M^-}(x, \theta) h(x). \quad (4)$$

Note that most prior works simplify eq. 3 to a shear, due to their local paraxial approximation, so that $\theta \approx \tan \theta$. While this allows the corresponding spectrum to be derived analytically (shear in angle), this may not be valid in our setting if the width w of each display unit is large compared to the distance to the barrier d . Fortunately, this does not modify the qualitative study of the lightfield spectrum which is now

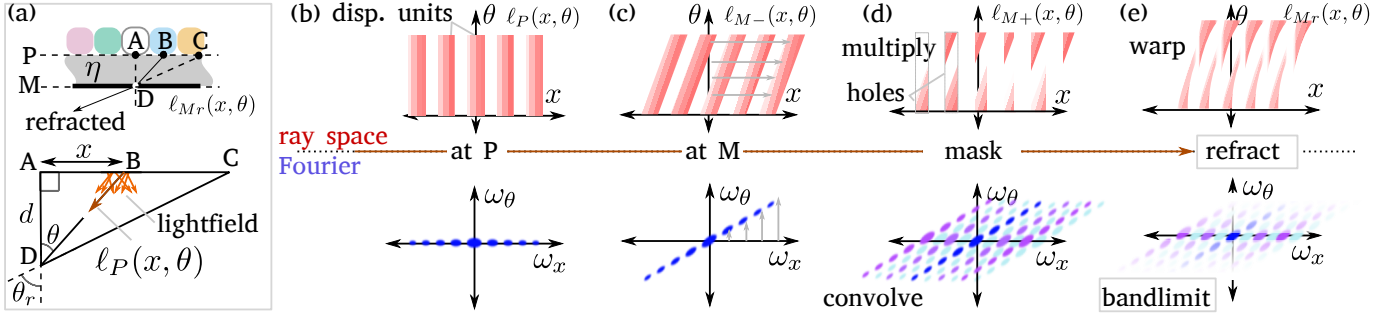


Figure 6: Frequency analysis of the warp introduced by refractive inserts.

stretched non-linearly (in θ) along the angular direction. Equation 4 is exactly as in prior work, and the product in ray space is equivalent to a convolution of the spectra on its rhs. Our contribution in this paper is the frequency analysis at a single refractive boundary (fig. 6.e).

The lightfield $\ell_{M+}(x, \theta)$ undergoes refraction at M and the resulting lightfield $\ell_{Mr}(x, \theta)$ is obtained as $\ell_{Mr}(x, \theta_r) = \ell_{M+}(x, \theta)$. Refraction at the plane M can be seen as a reparameterization in angle according to $\theta_r = \sin^{-1}\left(\frac{\sin \theta}{\eta}\right)$ (by Snell's law). Viewing this reparameterization as a composition of 1D functions (in angle only), and applying the result of Berger et al [2], we obtain a relationship between the bandwidths of $\hat{\ell}_{M+}(\omega_x, \omega_\theta)$, v_{M+} , and the bandwidths of $\hat{\ell}_{Mr}(\omega_x, \omega_\theta)$, v_{Mr} , as:

$$v_{Mr} = v_{M+} \max_{\theta} \left| \frac{d}{d\theta} \sin^{-1} \left(\frac{\sin \theta}{\eta} \right) \right| \quad (5)$$

$$\boxed{v_{Mr} = \frac{v_{M+}}{\eta}} \quad (6)$$

Equation. 6 shows that the bandwidth of the exitant, refracted lightfield $\hat{\ell}_{Mr}(\omega_x, \omega_\theta)$ is lower than the bandwidth of the unrefracted lightfield when refractive index (wrt air) of the insert is greater than one. View extraction is an angular slice of the lightfield, and therefore an angular projection in the Fourier domain. Therefore, images produced by our method are slightly more blurry (by a spectral scaling factor η) than without refractive inserts, but viewable from a wider range of angles.

3.4 Modified Parallel Group Rendering

We propose a simple modification of PGR which we call Modified Parallel Group Rendering (MPGR) to accommodate refractive inserts. Recall that the PGR approach divides pixels into groups and combines orthogonal projection matrix with an oblique projection matrix for each of the groups: $M_{PGR} = M_{view} M_{oblique} M_{ortho}$. If the plane of the barrier is considered to be $Z = 0$, M_{view} is decided by projection screen plane $z = d$ and $M_{oblique}$ depends on the direction of projection (see fig. 7).

$$M_{oblique} = \begin{bmatrix} 1 & 0 & 0 & 0 \\ 0 & 1 & 0 & 0 \\ -\frac{s}{d} & -\frac{t}{d} & 1 & 0 \\ 1 & 0 & 0 & 1 \end{bmatrix}, \quad (7)$$

where (s, t) is the coordinates of the rendered pixel P on the display unit and d is the optical distance. Although a different $M_{oblique}$ is required for each pixel group, they can be precomputed since the structure of the display is fixed.

Although refractive inserts introduce nonlinear bending of exiting rays (see ray from P to V_r in fig. 7), accommodating this effect can be done without raytracing. For this, we simply modify the projection matrix, leading to efficient rendering. We do this by identifying point P_v , which has identical st coordinates with P , by extending $\overline{O_h V_r}$. Due to the reciprocity of light, if we render virtual pixel P_v and display this result at P , light ray $\overline{O_h V_r}$ will contain the correct radiant energy. We

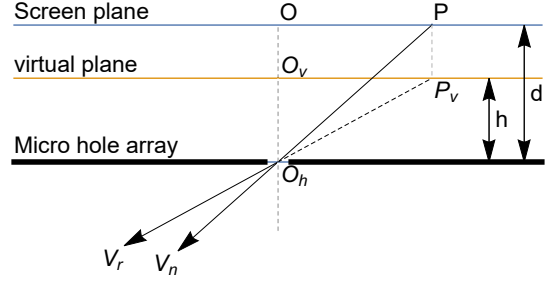


Figure 7: A ray from pixel P on the screen plane $Z = d$ passes through the hole O_h without along V_n without refraction and along V_r with refractive inserts. To modify PGR for our display (with refraction), we render a virtual pixel P_v which has the same st coordinates as P but is at $Z = h$ instead of $Z = d$ (for P). The result is rendered at P producing the desired exiting radiant energy. We do this by modifying the projection matrix thereby avoiding any expensive raytracing steps.

define a virtual projection plane $Z = h$ and render the virtual pixel P_v on it using PGR. Since P_v and P have the same st coordinates,

$$h = \frac{1}{\eta} \sqrt{(s^2 + t^2)(1 - \eta^2) + d^2}. \quad (8)$$

The view projection matrix is generated with $z = h$, by replacing d in Equation 7 by h for MPGR. The term in the square root is negative when total internal reflection occurs. The light from P does not go through micro hole O_h . So we do not render pixels if h is not real.

4 RESULTS AND DISCUSSION

We placed a parallax barrier with microholes in front of an LG 27UD68 LCD display which has a $597mm \times 336mm$ screen with 3840×2160 resolution (see fig. 9). The micro hole array was laser-cut from black self-sticky PVC sheet and the width of each micro hole is approximately $0.2mm$. Our refractive insert was a $3mm$ thick sheet of acrylic ($\eta = 1.3152$) and our prototype has an angular resolution $R_a = 36 \times 36$, with dimensions $w = 5.6mm \times 5.6mm$. The spatial resolution is $R_s = 106 \times 60$ (number of holes). We controlled the relative positioning of the micro holes and pixels using a frame with adjustable screws. The display was fixed onto a programmable turning table and measurements (photographs and video) were taken from different viewing angles.

4.1 Experiments

We present experiments that we performed to assess the resulting crosstalk, blur, brightness and errors due to misaligned barriers.

Crosstalk: We took photographs for every 3° within the observing angle range $[-180^\circ, 180^\circ]$. We visualize results for important angles in fig. 10. Angles and the corresponding rendered views (for reference) are shown in the first column, and a comparison of without (second column) and with refractive inserts (third column) is also shown. To

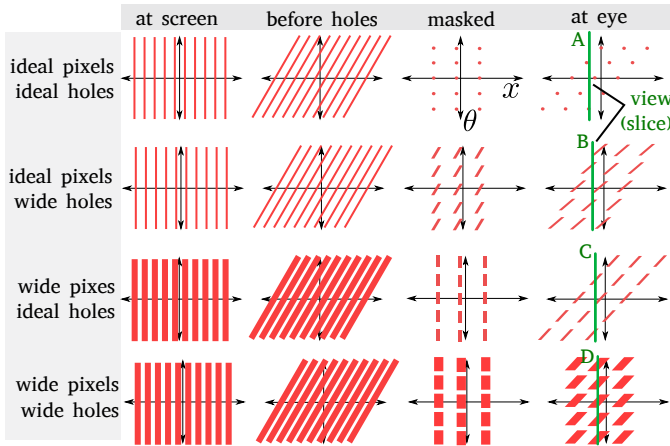


Figure 8: Illustration of different sources (rows) of blur through transport (columns) from a screen of displayed pixels to the eye. The view at any spatial location is an angular slice (green vertical line) of the lightfield at the eye (rightmost column). In cases B, C and D, there is spatial (horizontal) artifacts observable by moving the view slice to the left or right. In B and D, there is angular (vertical) spreading at any chosen view which will manifest as image blur. Refractive inserts introduce a non-linear warp after masking, before transport to the eye.

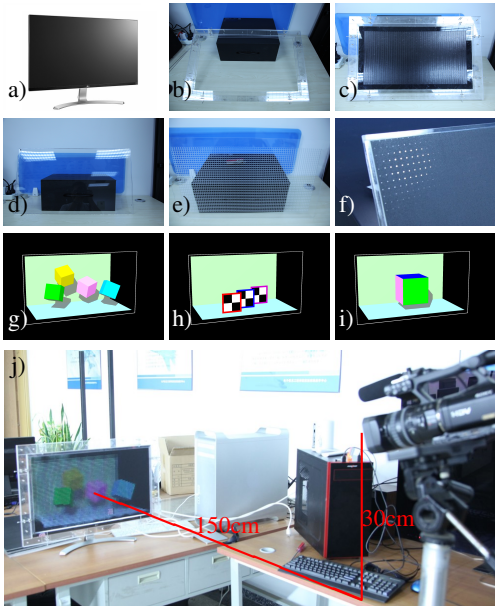


Figure 9: Experimental setup. a) Display screen used. b) Adjustable frame for positioning micro hole array. c) Frame with micro hole array. d) Refractive insert. e) The hollow panel with micro hole array (without refraction). f) The micro hole array, made of adhesive PVC, is attached to the refracting insert. g) Scene used for crosstalk experiments. h) Scene used for blurring experiments. i) Scene used for deformation experiments. j) The experimental setup.

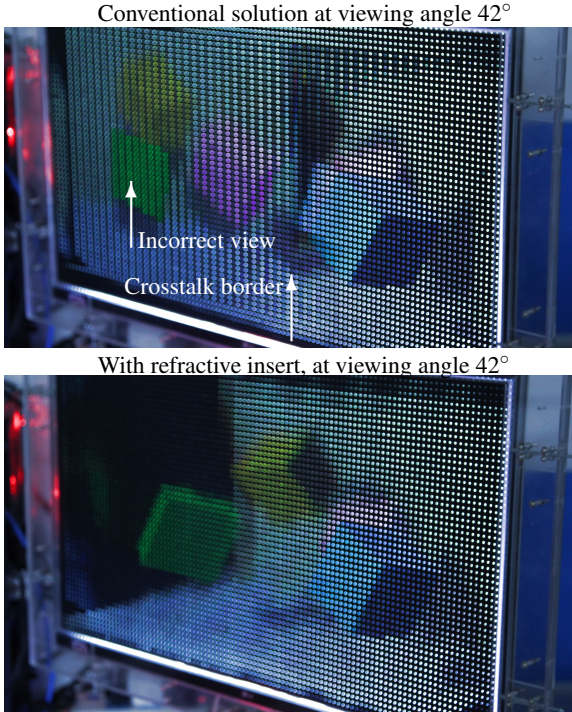
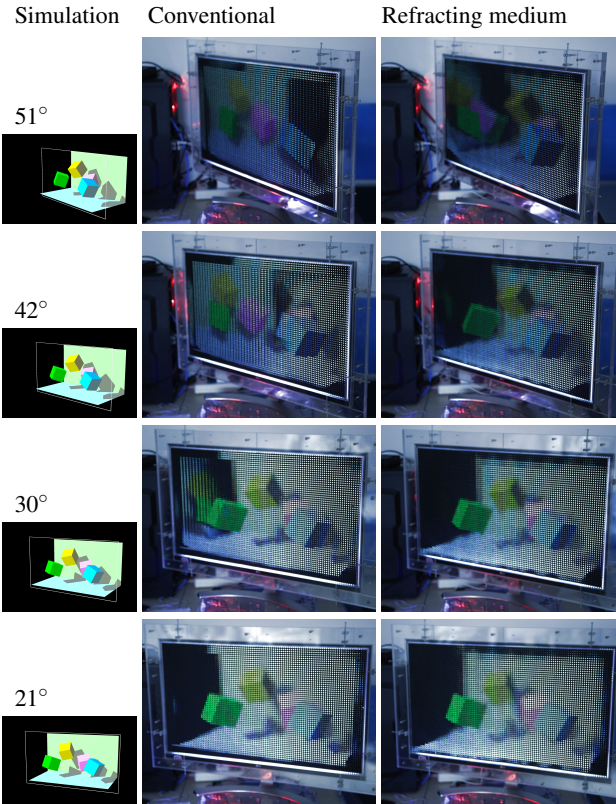


Figure 10: Photographs comparing our prototype (top, rightmost column) against the conventional display without refractive inserts (top, middle column). Rendered simulations are shown for reference (top, leftmost column). The effect of crosstalk is emphasized by an enlarged view of the row corresponding to a view angle of 42° . On the left side of the crosstalk border (overlaid white arrow), the displayed scene has incorrect perspective cues (see reference) due to crosstalk. These errors are less objectionable with refractive inserts (zoom in at the bottom). Even at larger angles (first row), refractive inserts avoid left-right perspective flipping. Best viewed on screen (zoom into pdf to avoid aliasing in pdf viewer).

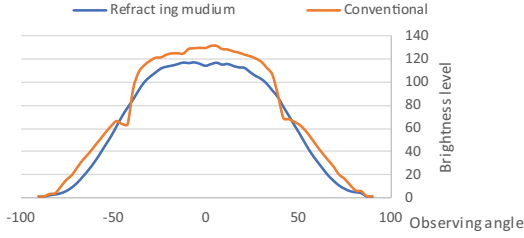


Figure 11: The curves of brightness level. Because the refracting medium is not one hundred percent transparent and the refraction extends the same amount of light to a wider operational angle, our prototype is slightly dimmer than the conventional solution while the observing angle is the same.

highlight the errors in the conventional solution at 42° , we show an enlarged version (top). Our prototype extends the viewing angle from 45° to 87° (increasing by 93%). It is noticeable that the error caused by out-of-bound crosstalk effect occurs from one side of the screen and grows as the absolute value of observing angle increases.

Brightness: We measured the brightness of the display as the value at the center pixel of each display unit, while displaying pure white pixels in a dark room. The curves are shown in fig. 11. Note that the brightness level of both display setups drops as the view angle approaches grazing. Our setup exhibits slightly reduced brightness. The steep drop in the conventional solution at around 45° is because about half of the spatial pixels within the sampled central area are blocked by our frame. Beyond this, severe crosstalk renders the conventional solution unusable anyway.

Blur: We assessed blur qualitatively as well as quantitatively. Blur results from a combination of the shallow depth of field due to large holes as well as due to finite sized pixels. First, we rendered a virtual checkerboard pattern at different depths and captured photographs of the display from different angles (see fig. 12). The red, blue and purple squares are $0cm$, $5cm$ and $10cm$ away from the micro hole array respectively. As expected, our method is as sharp for the object in the display plane but is slightly more blurry for objects away. At wider viewing angles our prototype performs better than without refraction. See sec. 4.2 for a quantitative discussion of blur.

Pixel mismatch: We studied the effects of three different kinds of mismatching which were introduced intentionally (see fig. 13) as: a) incorrect alignment of the microholes with their corresponding display units due to a translation; b) inconsistent sizes of the display unit and pitch of the holes in the parallax barrier (hole separation $595mm$ instead of $597mm$); and c) a slight rotation ($0.003rad$) of the parallax barrier. We call these translation, scale and rotational mismatching respectively.

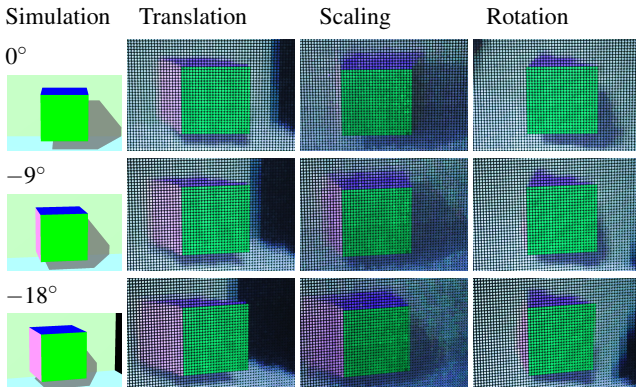


Figure 13: From left to right: rendered reference, translational mismatch, scaling mismatch, rotational mismatch.

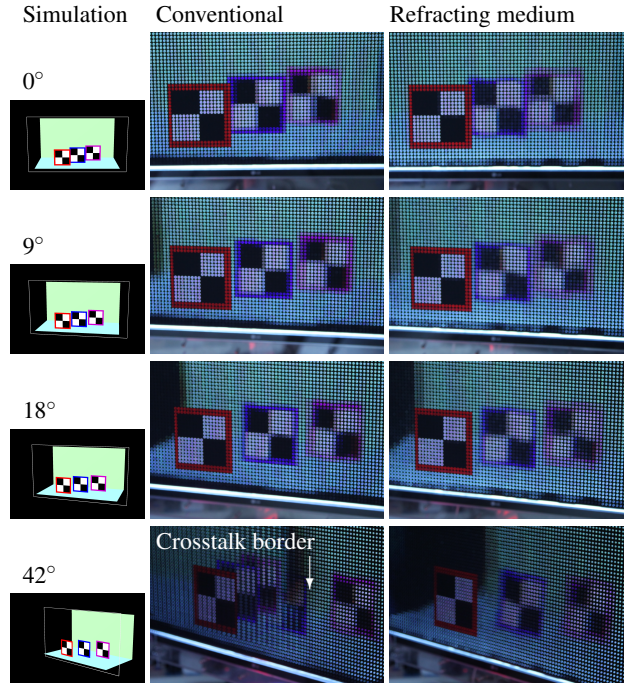


Figure 12: Blur effect experiment. Left: simulated scene. Middle: conventional solution. Right: our prototype with refracting medium. Note that both displays are affected by blurs so the squares with blue borders and purple borders are not so clear. The conventional solution suffers from out-of-bound crosstalk when observed from 42° . In contrast, our prototype works properly with acceptable blurring level while no crosstalk occurs.

4.2 Discussion

Crosstalk: Refractive inserts reduces crosstalk at wider viewing angles. In our prototype although we use a non-optimal $\eta = 1.3125$, there is a considerable reduction in crosstalk. Crosstalk is limited to the area where brightness is low (closer to grazing angle). Compared with introducing light barriers between spatial pixels, we have better spatial pixel density and angular spread. The conventional display operates well between -24° to 21° (45° viewing angle range) while our prototype operates between -45° to 42° , achieving a viewing angle range of 87° . We believe that the slight asymmetry is due to imprecision in the motor used to turn the monitor as well as the placement of the camera.

Blur: For a quantitative study of blur, we displayed a virtual light spot in 3D and simulated its blur due to finite sized pixels and holes. We estimated the blur radius at various viewpoints by simulation of visibility through a large pinhole of large pixels on the display screen. We also varied the position of the virtual object to understand the dependence of blur on distance from the display plane. We plot the angular blur size of a displayed virtual light spot against the view angle in figure 14 for virtual objects at different depths with ($\eta = 1.3$) and without refraction ($\eta = 1$). We also visualized the range of view angles with (wider region shaded blue) and without (narrow region shaded green) refraction. Interestingly, there is a fundamental difference between blur with and without refraction. Without refraction (dashed curves), blur is highest at normal viewing and gradually vanishes as the viewing approaches grazing. With refractive inserts however, the behavior is the opposite although the blur is relatively constant within the operational range of viewing angles (blue shaded region). We also generated heat maps of the angular blur size for multiple groups of pixel sizes (p) and hole sizes (b) as shown in figure 15. The virtual object was kept fixed at $10cm$ behind the display screen. The blur kernels are shown as insets.

Parameters: For the same micro hole size b and pixel size p , higher

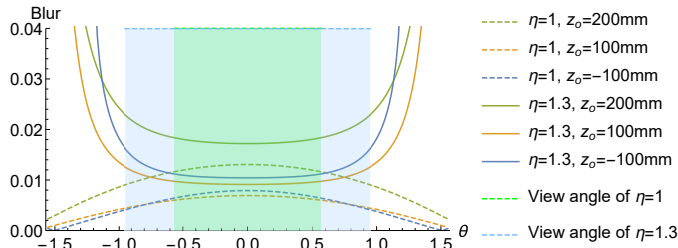


Figure 14: Blur size for virtual objects at different depths (z_o) for a viewer 1500mm away from the display center. $z_o > 0$ for the virtual objects behind the screen. The green area is the safe view angle ranges for $\eta = 1$ and the blue shaded area is that of our prototype with $\eta = 1.3$.

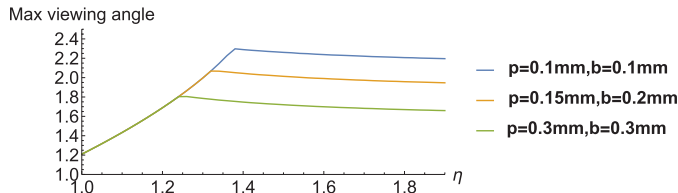


Figure 16: The simulated maximum viewing angle can be achieved for certain combination of η , b and p . When the blurring effect starts having serious effect, d is increased to ease the negative impact, so the max viewing angle does not drop so seriously.

refractive indices η introduces more blurring. As expected, smaller p and b alleviate blurring effects (see fig. 16). However, very small holes cause aberrations due to diffraction, which we have not considered in this paper. Increasing the thickness of the insert decreases the viewing angle but reduces blurring.

Rendering: We implemented two MPRGR pipelines which we call *low resolution projection* and *full resolution projection*. In low resolution projection, a collection of $u \times v$ oblique orthographic projection images whose resolutions are $s \times t$ are rendered then reassembled into an display unit array. Usually $uv \gg st$ so this approach is more efficient than rendering the display units one by one with modified perspective projection. The camera position is adjusted to $(0, 0, d_b - h)$. An extra rendering buffer is needed to store the intermediate rendering results and there is increased data transmission which could slow rendering. The resolution of each rendered images ($u \times v$) is low compared to the rendering zone ($us \times vt$) which introduces quantization errors. The resulting render exhibits a loss of high frequency information. Rendering shadow textures, for example, would be prone to aliasing. In full

	Conventional	With refraction
Diversity	Spatio-angular	Spatio-angular
Depth cues	Binocular	Binocular
Angular spread	$2 \arctan \frac{w}{2d}$	$2 \arcsin \frac{w\eta}{\sqrt{w^2+4d^2}}$
Brightness	$B_n(\theta)$	$\frac{\cos \theta}{\sqrt{\eta^2 - \sin^2 \theta}} B_n(\arcsin \frac{\sin \theta}{\eta})$
Deformation rate	$\frac{z}{d}$	$\frac{z}{d} \frac{[\frac{z}{d}(\eta^2-1)+\eta^2]^{3/2}}{\eta^2}$
Bandwidth	$\frac{4\pi^2}{pw}$	$\frac{1}{\eta} (\frac{4\pi^2}{pw})$
Angular resolution	$\frac{p}{w}$	$\frac{p}{w}$
Angular frequency	$\frac{2\pi d}{p \cos^2 \theta}$	$\frac{2\pi d}{p(1-\frac{1}{\eta^2} \sin^2 \theta)} \frac{\cos \theta}{\sqrt{\eta^2 - \sin^2 \theta}}$
Spatial resolution	$\frac{pN}{w}$	$\frac{pN}{w}$
Spatial frequency	$\frac{2\pi d}{p z }$	$\frac{2\pi d}{p z } \frac{\eta^2}{[\frac{z}{d}(\eta^2-1)+\eta^2]^{3/2}}$

Table 1: Comparison between conventional display and our prototype with refractive inserts. Derivations are presented in the appendix.

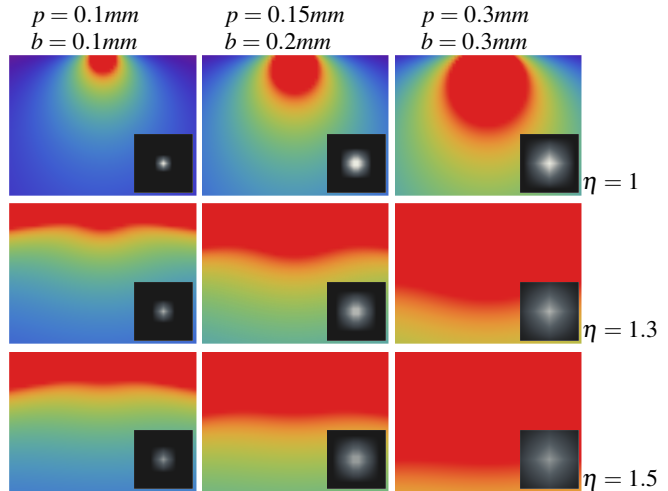


Figure 15: Simulation of 9 different combinations of pixel size p , hole size b and refractive index η . The display is at the top, middle of each of the heat maps ($3000mm \times 2250mm$) which visualize the extent of blur (red is high and blue is low). Insets show the blur kernel in a $20mm \times 20mm$ square when the viewer is $r = 1500mm$ in front of the display. The tolerable blur angle set in the simulation is $4w/r$.

resolution projection, we use the stencil buffer to mark the rendering area on the final rendering target (the display buffer) during each pass of the loop in figure 17. No extra data transmission or buffer is required during rendering. To render each frame, st passes of the loop are needed and each of them generates uv pixels of the final display units. These pixels are identical to pixels rendered in full resolution ($us \times vt$) but the rendering cost is closer to rendering its low resolution ($u \times v$) version. Although anti-aliasing via neighboring pixels cannot be applied in this case, the method is less prone to quantization errors. Due to its use of the stencil test, it introduces complication in the use of rendering algorithms which also exploit the stencil buffer (such as for shadows).

Limitations and future work: The main limitation of our prototype, as with any parallax barrier automultiscopic display, is its poor light efficiency. A further reduction in brightness can be attributed to the even distribution of the emitted light across a larger angular domain. It is possible to combine the idea of using refractive inserts with integral displays that use lenselet arrays. However, the engineering of such combinations is left as future work. The warping characteristics of such displays will need careful analysis. Further, the parameters under question are also different, since there will be two refractive indices that need to be chosen. Finally, embracing integral displays for improved light efficiency is accompanied by a cost of shallow depth of field. The trade-off between light efficiency and depth of field of integral images with refractive inserts is non-trivial to analyze and lies beyond the scope of this paper. We believe that this opens exciting avenues of research.

5 CONCLUSION

We have presented a detailed analysis of a simple modification to conventional automultiscopic displays that use parallax barriers. The insertion of a refractive medium between the screen and parallax barrier of such displays yields many advantages including uniform distribution of light in the angular domain and widening of the viewing angle. We have presented a frequency domain analysis to show that refractive inserts act as bandlimiting filters in the angular domain. This results in slight blurring, which we analyzed quantitatively using simulations and qualitatively using rendering. We built a prototype display and demonstrate the perception of depth using a video where the view angle is smoothly varied.

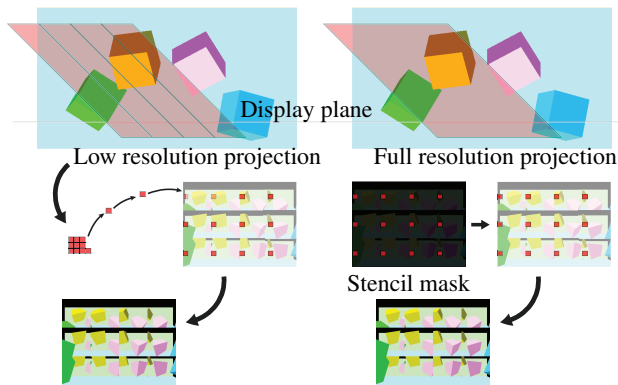


Figure 17: Method A (left) renders low resolution ($u \times v$) view images with parallel oblique orthographic projection during each pass of the loop, breaks the rendered image into pixels then render them to isolated positions respectively. Method B (Right) sets the stencil buffer to mask the rendering zone, so that the rendering process updates a collection of isolated pixels which have same *st* coordinates rather than all pixels of the display unit array during each pass of the loop.

ACKNOWLEDGMENTS

Kartic Subr was supported by a Royal Society University Research Fellowship.

REFERENCES

- [1] E. H. Adelson and J. R. Bergen. The plenoptic function and the elements of early vision. 1991.
- [2] S. Bergner, T. Moller, D. Weiskopf, and D. J. Muraki. A spectral analysis of function composition and its implications for sampling in direct volume visualization. *IEEE transactions on visualization and computer graphics*, 12(5), 2006.
- [3] A. Berthier. Images stéréoscopiques de grand format. *Cosmos*, 34(590):205–210, 1896.
- [4] J.-X. Chai, X. Tong, S.-C. Chan, and H.-Y. Shum. Plenoptic sampling. In *Proceedings of the 27th annual conference on Computer graphics and interactive techniques*, pp. 307–318. ACM Press/Addison-Wesley Publishing Co., 2000.
- [5] C.-W. Chen, M. Cho, Y.-P. Huang, and B. Javidi. Improved viewing zones for projection type integral imaging 3d display using adaptive liquid crystal prism array. *Journal of Display Technology*, 10(3):198–203, 2014.
- [6] M. Cho and J.-Y. Jang. Viewing angle enhancement of parallax barrier-based one-dimensional integral imaging display using a high refractive index medium. *Optik-International Journal for Light and Electron Optics*, 127(2):840–843, 2016.
- [7] N. A. Dodgson et al. Analysis of the viewing zone of multi-view autostereoscopic displays. In *Proc. SPIE*, vol. 4660, pp. 254–265, 2002.
- [8] S.-P. Du, P. Didyk, F. Durand, S.-M. Hu, and W. Matusik. Improving visual quality of view transitions in automultiscopic displays. *ACM Transactions on Graphics (TOG)*, 33(6):192, 2014.
- [9] F. Durand, N. Holzschuch, C. Soler, E. Chan, and F. X. Sillion. A frequency analysis of light transport. In *ACM Transactions on Graphics (TOG)*, vol. 24, pp. 1115–1126. ACM, 2005.
- [10] N. Efrat, P. Didyk, M. Foshey, W. Matusik, and A. Levin. Cinema 3D: large scale automultiscopic display. *ACM Trans. Graph.*, 35(4):59:1–59:12, 2016. doi: 10.1145/2897824.2925921
- [11] D. Fattal, Z. Peng, T. Tran, S. Vo, M. Fiorentino, J. Brug, and R. G. Beausoleil. A multi-directional backlight for a wide-angle, glasses-free three-dimensional display. *Nature*, 495(7441):348, 2013.
- [12] G. Favalora, R. K. Dorval, D. Hall, M. Giovinco, and J. Napoli. Volumetric three-dimensional display system with rasterization hardware. In *Proc. SPIE*, vol. 4297, pp. 227–235, 2001.
- [13] T. Fukiage, T. Kawabe, and S. NISHIDA. Hiding of phase-based stereo disparity for ghost-free viewing without glasses. *ACM Transactions on Graphics (TOG)*, 36(4):147, 2017.
- [14] A. Gershun. The light field. *Studies in Applied Mathematics*, 18(1-4):51–151, 1939.
- [15] B. Goldluecke and S. Wanner. The variational structure of disparity and regularization of 4D light fields. In *IEEE Conference on Computer Vision and Pattern Recognition (CVPR)*, 2013.
- [16] M. Halle. Autostereoscopic displays and computer graphics. *SIGGRAPH Comput. Graph.*, 31(2):58–62, May 1997. doi: 10.1145/271283.271309
- [17] M. W. Halle and A. Kropp. Fast computer graphics rendering for full parallax spatial displays. *Practical Holography XI*, 3011:105–112, 1997.
- [18] R. Horstmeyer, S. B. Oh, and R. Raskar. View-dependent displays and the space of light fields. *arXiv preprint arXiv:1008.0034*, 2010.
- [19] F.-C. Huang, D. Luebke, and G. Wetzstein. The light field stereoscope. *ACM SIGGRAPH 2015 Emerging Technologies on - SIGGRAPH '15*, pp. 1–1, 2015. doi: 10.1145/2782782.2792493
- [20] K.-C. Huang, Y.-H. Chou, L.-c. Lin, H. Y. Lin, F.-H. Chen, C.-C. Liao, Y.-H. Chen, K. Lee, and W.-H. Hsu. A study of optimal viewing distance in a parallax barrier 3d display. *Journal of the Society for Information Display*, 21(6):263–270, 2013.
- [21] F. E. Ives. Parallax stereogram and process of making same., Apr. 14 1903. US Patent 725,567.
- [22] J.-S. Jang and B. Javidi. Improvement of viewing angle in integral imaging by use of moving lenslet arrays with low fill factor. *Applied optics*, 42(11):1996–2002, 2003.
- [23] N. K. Kalantari, T.-C. Wang, and R. Ramamoorthi. Learning-based view synthesis for light field cameras. *ACM Transactions on Graphics (TOG)*, 35(6):193, 2016.
- [24] B. Krolla, M. Diebold, B. Goldluecke, and D. Stricker. Spherical light fields. In *British Machine Vision Conference (BMVC)*, 2014.
- [25] M. Lang, A. Hornung, O. Wang, S. Poulakos, A. Smolic, and M. Gross. Nonlinear disparity mapping for stereoscopic 3d. In *ACM Transactions on Graphics (TOG)*, vol. 29, p. 75. ACM, 2010.
- [26] D. Lanman, M. Hirsch, Y. Kim, and R. Raskar. Content-adaptive parallax barriers: optimizing dual-layer 3d displays using low-rank light field factorization. *ACM Transactions on Graphics (TOG)*, 29(6):163, 2010.
- [27] D. Lanman and D. Luebke. Near-eye light field displays. *ACM Transactions on Graphics (TOG)*, 32(6):220, 2013.
- [28] D. Lanman, G. Wetzstein, M. Hirsch, W. Heidrich, and R. Raskar. Polarization fields: dynamic light field display using multi-layer lcds. *ACM Transactions on Graphics (TOG)*, 30(6):186, 2011.
- [29] B. Lee, S. Jung, and J.-H. Park. Viewing-angle-enhanced integral imaging by lens switching. *Optics letters*, 27(10):818–820, 2002.
- [30] S. Lee, C. Jang, S. Moon, J. Cho, and B. Lee. Additive light field displays: Realization of augmented reality with holographic optical elements. *ACM Trans. Graph.*, 35(4):60:1–60:13, July 2016. doi: 10.1145/2897824.2925971
- [31] A. Levin, W. Freeman, and F. Durand. Understanding camera trade-offs through a bayesian analysis of light field projections—a revision. 2008.
- [32] M. Levoy and P. Hanrahan. Light field rendering. In *Proceedings of the 23rd annual conference on Computer graphics and interactive techniques*, pp. 31–42. ACM, 1996.
- [33] C.-K. Liang and R. Ramamoorthi. A light transport framework for lenslet light field cameras. *ACM Transactions on Graphics (TOG)*, 34(2):16, 2015.
- [34] G. Lippmann. Epreuves reversibles donnant la sensation du relief. *J. Phys. Theor. Appl.*, 7(1):821–825, 1908.
- [35] A. W. Lohmann and D. Paris. Binary fraunhofer holograms, generated by computer. *Applied Optics*, 6(10):1739–1748, 1967.
- [36] G. D. Love, D. M. Hoffman, P. J. Hands, J. Gao, A. K. Kirby, and M. S. Banks. High-speed switchable lens enables the development of a volumetric stereoscopic display. *Optics express*, 17(18):15716–15725, 2009.
- [37] A. MacQuarrie and A. Steed. Cinematic virtual reality: Evaluating the effect of display type on the viewing experience for panoramic video. In *2017 IEEE Virtual Reality (VR)*, pp. 45–54, March 2017. doi: 10.1109/VR.2017.7892230
- [38] B. Masia, G. Wetzstein, P. Didyk, and D. Gutierrez. A survey on computational displays: Pushing the boundaries of optics, computation, and perception. *Computers & Graphics*, 37(8):1012–1038, 2013.
- [39] W. Matusik and H. Pfister. 3d tv: a scalable system for real-time acquisition, transmission, and autostereoscopic display of dynamic scenes. *ACM Transactions on Graphics (TOG)*, 23(3):814–824, 2004.
- [40] J. C. Nelson and R. L. Brott. Autostereoscopic display with fresnel lens element and double sided prism film adjacent a backlight having a light transmission surface with left and right eye light sources at opposing ends modulated at a rate of at least 90 hz, July 6 2010. US Patent 7,750,982.
- [41] W. Plesniak and M. Halle. Computed holograms and holographic video

- display of 3d data. In *ACM SIGGRAPH 2005 Courses*, p. 69. ACM, 2005.
- [42] A. Sullivan. 58.3: A solid-state multi-planar volumetric display. In *SID symposium digest of technical papers*, vol. 34, pp. 1531–1533. Wiley Online Library, 2003.
- [43] J. Tompkin, S. Heinze, J. Kautz, and W. Matusik. Content-adaptive lenticular prints. *ACM Transactions on Graphics (TOG)*, 32(4):133, 2013.
- [44] J. Tompkin, S. Muff, J. McCann, H. Pfister, J. Kautz, M. Alexa, and W. Matusik. Joint 5D Pen Input for Light Field Displays. *Proceedings of the 28th Annual ACM Symposium on User Interface Software & Technology - UIST '15*, pp. 637–647, 2015. doi: 10.1145/2807442.2807477
- [45] M. Wang, X.-J. Zhang, J.-B. Liang, S.-H. Zhang, and R. R. Martin. Comfort-driven disparity adjustment for stereoscopic video. *Computational Visual Media*, 2(1):3–17, 2016.
- [46] T.-C. Wang, J.-Y. Zhu, N. K. Kalantari, A. A. Efros, and R. Ramamoorthi. Light field video capture using a learning-based hybrid imaging system. *arXiv preprint arXiv:1705.02997*, 2017.
- [47] S. Wanner and B. Goldluecke. Variational light field analysis for disparity estimation and super-resolution. *IEEE Transactions on Pattern Analysis and Machine Intelligence*, 36(3):606–619, 2014.
- [48] G. Wetzstein, D. Lanman, W. Heidrich, and R. Raskar. Layered 3d: tomographic image synthesis for attenuation-based light field and high dynamic range displays. In *ACM Transactions on Graphics (ToG)*, vol. 30, p. 95. ACM, 2011.
- [49] G. Wetzstein, D. Lanman, M. Hirsch, and R. Raskar. Tensor displays: compressive light field synthesis using multilayer displays with directional backlighting. 2012.
- [50] R. Yang, X. Huang, S. Li, and C. Jaynes. Toward the light field display: Autostereoscopic rendering via a cluster of projectors. *IEEE Transactions on Visualization and Computer Graphics*, 14(1):84–96, 2008. doi: 10.1109/TVCG.2007.70410
- [51] S. K. Yoon, S.-K. Kim, and H. Ju. Reduction of optical aberration induced by refraction of light in a parallax barrier based autostereoscopic 3d display. *Optics Communications*, 392:135–141, 2017.
- [52] Z. Zhou, T. Yu, X. Qiu, R. Yang, and Q. Zhao. Light field projection for lighting reproduction. In *2015 IEEE Virtual Reality (VR)*, pp. 135–142, March 2015. doi: 10.1109/VR.2015.7223335
- [53] M. Zwicker, W. Matusik, F. Durand, and H. Pfister. Antialiasing for automultiscopic 3d displays. In *Proceedings of the 17th Eurographics Conference on Rendering Techniques*, EGSR '06, pp. 73–82. Eurographics Association, Aire-la-Ville, Switzerland, Switzerland, 2006. doi: 10.2312/EGWR/EGSR06/073-082

APPENDIX

We derive results for are one spatial pixel (display unit along with its micro hole) and consider a virtual object at (x, z) which is rendered as one pixel (x_p, d) on the display unit. Without refraction, let the pixel be visible along angle θ . Let the angle of incidence from the display to the barrier be $\theta_n = \theta$ for displays without the inserts and $\theta_r = \arcsin(\sin(\theta)/\eta)$ (by Snell's law) for displays with refractive inserts.

Brightness: Let the radiance emitted by the automultiscopic display be $B_n(\theta)$ and $B_r(\theta)$ without and with refractive inserts respectively. The energy (irradiance) within a narrow light beam (with spread $\Delta\theta$) is $\Delta\theta B_n(\theta)$, and by conservation of energy $\Delta\theta_n B_n(\theta_n) = \Delta\theta B_n(\theta)$. If the insert does not behave as a participating medium, that is it does not scatter or absorb energy, then the corresponding equation with refractive inserts is $\Delta\theta_r B_n(\theta_r) = \Delta\theta B_r(\theta)$, so in the limit

$$B_r(\theta) = \lim_{\Delta\theta \rightarrow 0} \frac{\Delta\theta_r}{\Delta\theta} B_n(\theta_r) = \frac{\partial\theta_r}{\partial\theta} B_n(\theta_r) \quad (9)$$

$$= \frac{\cos\theta}{\sqrt{\eta^2 - \sin^2\theta}} B_n(\arcsin \frac{\sin\theta}{\eta}) \quad (10)$$

Pixel mismatch: The perception of depth crucially depends on alignment between pixels and the holes in the barrier. We derive the translational displacement error Δx of a virtual object located at (x, z) caused by mismatching Δx_p of pixel (x_p, d) . We use mismatch rate $\partial x/\partial x_p$ to describe how sensitive the apparent sliding of the virtual object is to

the positioning of barriers. Without refraction, $x/z = x_p/d$, therefore

$$\frac{\partial x}{\partial x_p} = \frac{z}{d} \quad (11)$$

With refractive inserts, we have

$$\sin \arctan \frac{x}{z} = \eta \sin \arctan \frac{x_p}{d} \quad (12)$$

$$\frac{x}{x_p} = \frac{1}{d} \sqrt{\eta^2(x^2 + z^2) - x^2} \quad (13)$$

$$\frac{\partial x}{\partial x_p} = \frac{z}{d} \frac{[\frac{x^2}{z^2}(\eta^2 - 1) + \eta^2]^{3/2}}{\eta^2}. \quad (14)$$

Spatial and angular resolution: Since pixels in a display unit are spread apart evenly, the spatial frequency $\omega_p = 2\pi/p$. Since the spatial resolution does not depend on depth, the spatial frequencies satisfy $\omega_x \Delta x = \omega_p \Delta x_p$, so

$$\omega_x = \frac{\partial x_p}{\partial x} \omega_p, \quad (15)$$

$$= \frac{2\pi d}{pz}. \quad (16)$$

since $x_p = xd/z$ without refraction. With refractive inserts, since

$$x_p = \frac{xd}{\sqrt{\eta^2 - 1x^2 + \eta^2 z^2}}, \quad (17)$$

we obtain

$$\omega_x = \frac{2\pi d}{p|z|} \frac{\eta^2}{[\frac{x^2}{z^2}(\eta^2 - 1) + \eta^2]^{3/2}}. \quad (18)$$

Angular resolution is nonlinear in θ , for farfield viewing, even without refractive inserts. Since $x_p = d \tan \theta$ and $\omega_\theta \Delta \theta = \omega_p \Delta x_p$, we have

$$\omega_\theta = \lim_{\Delta\theta \rightarrow 0} \omega_p \frac{\Delta x_p}{\Delta \theta} = \omega_p \frac{\partial x_p}{\partial \theta} \quad (19)$$

$$= \frac{2\pi d}{p \cos^2 \theta} \quad (20)$$

With refractive inserts, $x_p = d \tan \arcsin \frac{\sin \theta}{\eta}$, which leads to

$$\omega_\theta = \frac{2\pi d}{p(1 - \frac{1}{\eta^2} \sin^2 \theta)} \frac{\cos \theta}{\sqrt{\eta^2 - \sin^2 \theta}}. \quad (21)$$